

# Imaging Coulomb Islands in a Quantum Hall Interferometer

B. Hackens<sup>1</sup>, F. Martins<sup>1</sup>, S. Faniel<sup>1</sup>, C. A. Dutu<sup>2</sup>, H. Sellier<sup>3</sup>,  
S. Huant<sup>3</sup>, M. Pala<sup>4</sup>, L. Desplanque<sup>5</sup>, X. Wallart<sup>5</sup>, V. Bayot<sup>1,3</sup>

<sup>1</sup> *Institute of Condensed Matter and Nanosciences - Nanophysics (IMCN/NAPS),*

*Université catholique de Louvain,*

*B-1348 Louvain-la-Neuve, Belgium*

<sup>2</sup> *Information and Communication Technologies,*

*Electronics and Applied Mathematics (ICTEAM),*

*Université catholique de Louvain,*

*B-1348 Louvain-la-Neuve, Belgium*

<sup>3</sup> *Institut Néel,*

*CNRS and Université Joseph Fourier,*

*BP 166, 38042 Grenoble cedex 9, France*

<sup>4</sup> *IMEP-LAHC, Grenoble INP,*

*Minatec, 3 Parvis Louis Néel,*

*38016 Grenoble, France*

<sup>5</sup> *IEMN, Cité scientifique,*

*Villeneuve d'Ascq, France*

(Dated: October 25, 2018)

## Abstract

In the Quantum Hall regime, near integer filling factors, electrons should only be transmitted through spatially-separated edge states. However, in mesoscopic systems, electronic transmission turns out to be more complex, giving rise to a large spectrum of magnetoresistance oscillations. To explain these observations, recent models put forward that, as edge states come close to each other, electrons can hop between counterpropagating edge channels, or tunnel through Coulomb islands. Here, we use scanning gate microscopy to demonstrate the presence of quantum Hall Coulomb islands, and reveal the spatial structure of transport inside a quantum Hall interferometer. Electron islands locations are found by modulating the tunneling between edge states and confined electron orbits. Tuning the magnetic field, we unveil a continuous evolution of active electron islands. This allows to decrypt the complexity of high magnetic field magnetoresistance oscillations, and opens the way to further local scale manipulations of quantum Hall localized states.

PACS numbers: 73.21.La,73.23.Ad,03.65.Yz,85.35.Ds

The quantum nature of electrons is two-sided: discreteness of charge and wave-like behaviour. Most of the time, experiments reveal either one or the other. Quantum rings (QR) are known to be archetype devices where the wave-like nature of electrons manifests itself through Aharonov-Bohm (AB) oscillations [1]. They originate from the  $B$ -dependence of the phase acquired by electrons along the QR's arms, which modulates electron interferences within the QR. Therefore, in the coherent regime of transport and at low magnetic field  $B$ , the resistance of a mesoscopic quantum ring exhibits oscillations as  $B$  is varied, with a flux period corresponding to the flux quantum  $\phi_0 = h/e$  [2].

On the other hand, charge quantization can dramatically affect transport through a nanoscopic island occupied by  $N$  electrons. When the charging energy  $e^2/C \gg k_B T$ , where  $C$  is the island capacitance, Coulomb blockade (CB) prohibits electron transport except for potential values such that  $N$  and  $N + 1$  states are degenerate [3]. CB manifests itself by periodic conductance peaks when the electrostatic potential is varied.

By contrast, in the quantum Hall regime, the situation should be simpler : the resistance vanishes at low temperature since transport occurs through edge states [4–6]. Several local-probe experiments have confirmed this edge-state picture and imaged localized states in the bulk of macroscopic two-dimensional electron systems [7–10]. However, numerous experiments on mesoscopic devices in the quantum Hall regime revealed surprising observations, such as pseudo-Aharonov-Bohm "subperiods" and "superperiods" [11–17]. Motivated by these unexpected results, recent theories brought to the fore the discrete nature of electrons to explain the broad range of periodicities. They invoke Coulomb interactions and tunneling between an electron island and edge states [18] (Fig. 1), which may be combined with a spatial oscillation of the outermost electron orbit in the island [17]. Complementing these theories, simulations yielded a detailed microscopic description of the different possible processes taking place in this regime [19, 20]. To the theoretical debate adds the diversity of experimental observations, which hampers unambiguous determination of the precise mechanisms at play at the local scale.

Here, we present a spatially-resolved investigation of electron transport inside an interferometer formed by an InGaAs/InAlAs quantum ring (see method section), driven in the integer quantum Hall (QH) regime. We show that each pseudo-AB period can be associated with a specific Coulomb island formed by edge states loops enclosing a hill or a valley in the potential. Each active Coulomb island can be located precisely inside the QR by tuning the

magnetic field and imaging the spatial shift of Coulomb resonances by means of scanning gate microscopy.

## Results

**Magnetoresistance measurements.** At low  $B$  and  $T$ , electron transport through the QR is in the coherent regime. This is attested by periodic Aharonov-Bohm oscillations in resistance  $R$  vs  $B$ . As expected, the AB period  $\Delta B_{\text{AB}} = 9$  mT (Fig. 2c), corresponds to the average QR radius (380 nm). Note also that the QR is in the quasi-ballistic regime (the electron mean free path is  $\sim 800$  nm at low  $B$ ), and  $\sim 25$  transverse modes are transmitted through the QR's openings (the Fermi wavelength is 22 nm, and the openings' width is 250 nm). At high- $B$ , the two-dimensional electron system enters into the QH regime and its transverse magnetoresistance  $R_{xy}$  vs  $B$  exhibits plateaus at values  $h/(\nu e^2)$ , where  $\nu$  is the (integer) filling factor (Fig. 2a). Within the plateaus, the Hall bar longitudinal magnetoresistance  $R_{xx}$  vs  $B$  drops to zero. In contrast, in the  $B$ -range coinciding with the position of the plateaus, the magnetoresistance of the QR displays strong reproducible fluctuations with a wide range of characteristic  $B$ -scales (Fig. 2b-f). On Fig. 2b, we also note the absence of finite resistance plateaus, which would indicate a difference in the number of filled Landau levels in the bulk and in the constrictions [15]. A closer look at  $R$  vs  $B$  in the region near  $\nu = 6$  reveals high-frequency periodic oscillations over some parts of the high  $B$ -range (Fig. 2f), with a period  $\Delta B = 1.5$  mT much smaller than the AB oscillations. Fig. 2e shows that a similar pattern is also visible on the plateau near  $\nu = 8$ , but with an even shorter period  $\Delta B = 1.1$  mT. Finally, these high- $B$  oscillations rapidly decay with temperature (Fig. 2e-f) and vanish before reaching 1 K. This contrasts with AB oscillations that, like the phase coherence time, saturate below  $\sim 1$  K [21] and are still visible at 2.5 K (Fig. 2c). An alternative mechanism, unrelated to electron interferences, must therefore be invoked to explain our observations.

To explain the presence of subperiod oscillations, a recent theory invokes Coulomb blockade of electrons tunneling between the conducting edge states transmitted along the borders of the QR and those forming a quantum Hall electron island located at the center of the device [18] (Fig. 1). Changing the magnetic field redistributes electrons within the Landau levels (LLs): if the flux through the area  $A$  enclosing the island increases by one flux quantum

$\phi_0$ , one electron must be added to each filled LLs. This process introduces a new contribution to the island charging energy, with a magnetic field period  $\Delta B = (\phi_0/A)/f_c = \Delta B_{AB}/f_c$ , where  $f_c$  is indeed the number of filled LLs. In turn, charging energy oscillations affect the QR resistance through the Coulomb blockade of electrons tunnelling between the quantum Hall island and the transmitted edge states. Note that the area encircled by edge states at high  $B$  is not necessarily equal to the mean area  $A$  of the QR, which determines  $\Delta B_{AB}$ . Simulations (not shown here) of the electron local density of states at  $B = 9.5$  T in a 2DEG with the same Fermi energy as in the experiment, indicate that the outermost populated edge state extends 55 nm away from the edge of the device. Taking this value and edge roughness into account, an edge state loop encircling the central QR antidot would therefore have a radius similar to the QR mean radius. This explains the remarkable consistency between the prediction of pseudo-AB subperiods  $\Delta B_{AB}/f_c$  and our observations  $\Delta B = 1.5$  mT and 1.1 mT at  $\nu = 6$  and  $\nu = 8$ , respectively (Fig. 2e-f).

From the analysis of the QR magnetoresistance oscillations, a quantum Hall Coulomb island should therefore be present in our quantum ring. While our sample geometry is *a priori* well suited to generate a quantum island around the central antidot, it could, as we will see later, locate elsewhere. Therefore local-scale information is needed to strengthen our understanding. In addition, the observation of subperiod oscillations only in narrow  $B$ -windows remains to be explained.

**Scanning gate microscopy.** Combining electron transport measurements with local probe techniques has already proven powerful to investigate the local details of electron behaviour inside various mesoscopic systems such as quantum point contacts [22–24], open and closed quantum dots [25–27] and quantum interferometers in the Aharonov-Bohm regime [28–31]. The technique, namely the scanning gate microscopy (SGM), consists in scanning the electrically-biased tip of an atomic force microscope in a plane parallel to the 2DES and recording the changes in the QR resistance,  $R(x, y)$ , induced by the tip located at  $(x, y)$ . In the context of the present experiments, the intrinsic sensitivity of Coulomb blockade to potential variations, makes SGM potentially well-suited to explore Coulomb islands.

In the  $B$ -range where subperiod oscillations were evidenced, the resistance map  $R(x, y)$  reveals a first set of concentric fringes (type-I) centered on the QR antidot (Fig. 3a). Qualitatively, this is exactly the behaviour expected for a gate scanning above an electron island experiencing Coulomb blockade, *i.e.* fringes correspond to isopotential lines located at con-

stant distances from the island [26, 27]. It is worth noting that it is indeed the flux through the edge state loop that controls the present CB effect. Hence, it can be tuned either by sweeping  $B$  or by approaching a negatively-polarized tip which raises the potential and enlarges the loop surface. Each concentric type-I fringe in Fig. 3a can therefore also be viewed as an *isoflux* line, that marks one single CB state. Note that the observed succession of concentric fringes is reminiscent of patterns evidenced in previous SGM experiments on a QR at low- $B$  [28], but the physical origin is totally different. As they vanish with increasing  $T$ , type-I fringes leave more apparent a second set of fringes (type-II), which is found  $T$ -independent below 1 K (Fig. 3b-c). The presence of two distinct phenomena is made even clearer on Fig. 3d, representing the  $T$ -dependence of  $\delta R$ , the standard deviation of  $R(x, y)$  in the rectangular regions labeled A and B on Fig. 3c, which are mainly encompassing type-I and type-II fringes, respectively.

## Discussion

Focusing on type-I fringes we note that they exhibit the same  $T$  dependence as the sub-period oscillations in the magnetoresistance (Fig. 3d). More precisely, the  $T^{-1}$  dependence of  $\delta R$  is compatible with a Coulomb blockade (CB) origin for both observations. Indeed, in classical CB experiments at  $B = 0$  T, the conductance peak height was reported to scale as  $\delta G \propto T^{-1}$  [3, 32], in the case of single-level transport through a lateral quantum dot. In our case, electrons transmitted through Coulomb islands contribute only to a part of the total conductance ( $\delta G/G \approx \delta R/R \lesssim 0.1$ ). Therefore,  $\delta R$  and  $\delta G$  should effectively exhibit the same  $T$  dependence.

Different frameworks can be invoked to explain the origin of type-II fringes. First, in the QH regime, potential variations are at the origin of 'hot spots', *i.e.* regions of high sensitivity of the resistance to local potential changes, which have been evidenced by SGM in a Hall bar at 1.9 K [33]. This may explain type-II patterns observed *within the area of the QR*. But the concentric ring-like patterns at the QR opening (region A, Fig. 3c) cannot be explained within this model, as 'hot spots' do not give rise to an oscillatory behaviour of the resistance when the tip approaches the spot. As an alternative, we suggest that the tip can modulate tunneling processes between counterpropagating edge states [18] at the openings. Affecting more than one edge state with the tip potential would induce the

observed concentric pattern. Magnetoresistance measurements could confirm this scenario : indeed,  $R$  vs  $B$  should exhibit finite resistance plateaus in the case of a tip-induced difference in the number of filled Landau levels inside the QR and at the openings [15].

Up to now, we have only analyzed a small  $B$ -range where  $\Delta B_{AB}/f_c$  subperiods dominate. A close look at Fig. 2d reveals that changing the magnetic field only by a few percents (*e.g.* from 9.5 to 9.7 T) dramatically modifies the magnetoresistance. This time, marked AB-like 'superperiod' oscillations show up, with  $\Delta B = 17$  mT (Fig. 4a), which share the same  $T^{-1}$  dependence (not shown) as the subperiods discussed above. According to the Rosenow-Halperin model [18], the superperiod oscillations indicate much smaller edge state loops. With an enclosed area  $A = (\phi_0/\Delta B)/f_c = 4 \times 10^{-14}$  m<sup>2</sup>, the loop should have a mean radius of  $\sim 65$  nm, and hence be located somewhere into the 300 nm-wide QR's arms. Our scanning gate should therefore be able to locate the loop.

The SGM localization is achieved in the sequence of Fig. 4b-d. From 9.75 to 9.65 T, fringes shrink and finally reveal the active Coulomb island, marked by the arrow on Fig. 4b. Note that the precise shape of the central SGM pattern is a convolution of the Coulomb island and tip potential shapes [34]. A more detailed view of this process is shown in Fig. 4e, displaying the  $B$ -dependence of the SGM profile taken along the dashed line in Fig. 4d, crossing the center of the fringes. Clearly, iso-resistance lines shift towards lower  $B$  as the negatively-charged tip approaches. Interestingly, the sign of the  $B$ -shift can indeed discriminate between edge states surrounding a potential hill and those confined on the border of the potential well. Assuming that the incompressible island surrounds a potential hill, approaching a negative-biased tip will raise the potential and increase the loop surface. If the incompressible island were localized in a potential well, the tip would reduce the loop surface. Since iso-resistance lines correspond to iso-flux states through the incompressible loop, the low- $B$  shift in Fig. 4e unambiguously identifies that the loop surrounds a potential hill.

It is worth noting that both subperiods and superperiods are observed in limited  $B$ -ranges. This means that a small potential perturbation by the tip could completely wipe out the CB oscillations, by either suppressing tunneling channels or suppressing CB islands. The region delimited by the dashed lines in Fig. 4e provides an example of such a state where AB-like superperiods are suppressed.

At first sight, the data taken near  $\nu = 10$  and shown in Fig. 5a resembles more SGM

maps presented in another QR but at low  $B$  [28]. Strikingly, the  $B$ -dependence of the profile taken along the yellow dashed line in Fig. 5a shows dominant oscillations with  $\Delta B \sim 7.8$  mT (Fig. 5c), very close to what the orthodox AB effect would provide in our sample. But the temperature dependence, shown in Fig. 5b, is not that expected for the AB effect. Indeed, the observed resistance oscillations are only pseudo-AB ones as they exhibit the same  $T^{-1}$ -dependence as sub and superperiod oscillations, indicating that they share the same Coulomb blockade origin.

As already shown near  $\nu = 6$ , the CB resonances shift towards low- $B$  when the tip approaches the QR (Fig. 5c). However, the relative amplitude of this shift is smaller compared to Fig. 4e because the tip does not scan directly over the active Coulomb island, so the potential perturbation experienced by the Coulomb island is not as large as in Fig. 4e. In addition, the data reveal a much richer pattern of fringes indicating that multiple Coulomb islands are at work. This is confirmed in Fig. 5d that shows the  $V_{tip}$  dependence of SGM profiles taken along the white dashed line on Fig. 5a (note that changing the position of the SGM profile yields qualitatively similar results). The main features are parabolic-like iso-resistance lines, indicated by the dashed lines. Their curvature evolves from zero at  $V_{tip} = 0$  V to positive or negative, according to the polarity of the tip, as expected for Coulomb interaction between the tip and a potential hill (see also ref. [27]). However, Fig. 5d, like Fig. 5c, also shows steeper resistance lines confirming the richness and complexity of mesoscopic transport in quantum Hall interferometers.

The wealth of behaviours exhibited in SGM data at different magnetic fields and tip voltages illustrates the capability of SGM to embrace the complexity of quantum Hall interferometers at the local scale, and, beyond that, of mesoscopic transport. The fine tuning of the local scale potential by the biased tip offers various opportunities to image and manipulate localized electron states. Such a detailed probing of electron transport in quantum Hall interferometers may also prove valuable in future explorations of non abelian quantum states [35, 36].

## Methods

**Device fabrication and sample parameters.** The quantum ring was patterned using electron beam lithography and wet etching in an InGaAs/InAlAs heterostructure [37]. A



two-dimensional electron system is confined 25 nm below the surface and its low temperature electron density and mobility are  $1.4 \times 10^{16} /\text{m}^2$  and  $4 \text{ m}^2/\text{Vs}$ , respectively, calculated from longitudinal and transverse magnetoresistance ( $R_{xx}$  and  $R_{xy}$  vs  $B$ , Fig. 2a) measurements on a Hall bar patterned next to the QR. The quantum ring inner and outer lithographic radii are 215 nm and 520 nm, respectively, and the width of both openings is 300 nm (Fig. S2). Note that the depletion length at the edge of etched trenches is  $\sim 25$  nm.

**SGM technique.** The experiments are carried out down to 100 mK with the sample thermally anchored to the mixing chamber of a  $^3\text{He}/^4\text{He}$  dilution refrigerator, and a home-made Atomic Force Microscope (AFM) suspended underneath. The force sensor consists in a commercial AFM cantilever coated with 20 nm of Ti and 10 nm of Pt (model CSC17 from MikroMasch; nominal tip radius : 40 nm), glued on one prong of a quartz tuning fork using conductive silver epoxy (Fig. S1a). To measure the sample topography, the AFM is operated in the dynamic mode with a feedback loop on the tuning fork oscillation frequency shift.

Using this method, we obtained the topography image of the quantum ring shown in Fig. S2a, at a temperature  $T = 100$  mK. Clear edges are visible where the heterostructure was etched, which is an indication of a sharp tip. Further information on the quality of both the tip and the imaging technique can be inferred by comparing the topography image (Fig. S2a) with Fig. S2b, obtained by Scanning Electron Microscopy (SEM) before cooling down the sample. Small differences can be observed between Fig. S2a and b. In particular, the size of the etched trenches is  $\sim 100$  nm smaller in the AFM topography. This discrepancy originates from the convolution of the tip shape with the surface topography in the AFM picture. Fig. S1b shows an image of the extremity of the tip used in the experiments presented in this work, obtained by SEM after the end of the SGM experiments. The size of the tip apex on this picture is  $\sim 70$  nm, which explains the difference in dimensions between Fig. S2a and b.

After imaging the topography of the ring, the tip is lifted at a distance of  $\sim 50$  nm from the sample surface (*i.e.* 75 nm away from the 2D electron system), and a bias voltage  $V_{\text{tip}}$  is applied on the tip in order to induce a local electrostatic perturbation for electrons transmitted through the QR. The quantum ring resistance  $R$  is measured using a low frequency (28 Hz) lock-in technique with a source-drain voltage across the QR always less than  $kT/e$ . Figures 4b-d were measured over several hours. Before and after such a set of SGM experi-

ment, the QR topography was imaged in order to check if the tip drifted with respect to the QR position during the experiment. We observed that the lateral drift was always smaller than 50 nm.

An additional shift between the topography and the  $R(x, y)$  map may originate from differences between the topographic tip and the "electric tip", *i.e.* the perturbation of electrostatic potential associated with the charged tip, experienced by electrons inside the quantum ring. Indeed, charged contamination on both the tip or the sample surface may contribute to alter this potential. This shift can be roughly estimated by noting that each set of concentric resistance fringes in the  $R(x, y)$  maps is centered on a Coulomb island, and must therefore have its center located within the limits of the quantum ring. By examining all the available  $R(x, y)$  maps, we could determine a higher bound of  $\sim 150$  nm on this shift (*i.e.* a shift larger than 150 nm would mean that some sets of resistance fringes are centered outside the QR area).

A crucial issue in the context of scanning gate microscopy is the "gating behaviour" of the tip [34, 38]. First, Fig. S1b shows that the metal layer covering the tip apex remained continuous during our experiment, and was not damaged by the numerous topographic scans realized at low temperature. In addition, there is no indication for a multiple tip, neither in Fig. S1b, nor in topography mode, nor in SGM images. Complementary, the electrical quality of the tip can be evaluated from the  $R(x, y)$  maps. In the  $R(x, y)$  map shown in Fig. S3, neighboring resistance fringes separated by less than  $\sim 50$  nm can be distinguished, which gives an indication on the width of the perturbing potential. Note that this width increases with the tip-surface separation in SGM mode.

Furthermore, the electrical potential associated with the charged tip should ideally have a circular symmetry, in order to avoid unwanted distortion of the features visible in the  $R(x, y)$  map. This symmetry can be evaluated on SGM maps of quantum dots: when the tip potential shifts an energy level of the quantum dot in resonance with the source and drain energy levels, electrons can tunnel through the quantum dot, which induces a current rise. In an SGM map, these resonances are visible as sets of concentric rings. The set of rings is directly related to the electrical potential of the tip, as shown in ref. [34]. In our experiment, the sets of resistance fringes in  $R(x, y)$  maps are also related to the Coulomb blockade phenomenon, and correspond to isopotential lines. Their precise shape depends both on the tip potential shape, and on the shape of the potential hill around which each

electron loop is localized. In the case of an anisotropic tip potential, the sets of resistance fringes in  $R(x, y)$  maps would all exhibit the same shape distortion related to the potential anisotropy. This is contrary to our observations: we observe a large diversity in the shapes of resistance fringes, but no recurrent anisotropy. This indicates that the tip potential shape is not anisotropic.

- 
- [1] Aharonov, Y. & Bohm, D. Significance of Electromagnetic Potentials in the Quantum Theory, *Phys. Rev.* **115**, 485-491 (1959).
  - [2] Webb, R. A., Washburn, S., Umbach, C. P. & Laibowitz, R. B. Observation of  $h/e$  Aharonov-Bohm Oscillations in Normal-Metal Rings, *Phys. Rev. Lett.* **54**, 2696-2699 (1985).
  - [3] Kouwenhoven, L. P., Marcus, C. M., McEuen, P. L., Tarucha, S., Westervelt, R. M. & Wingreen, N. S. Electron transport in quantum dots, in *Mesoscopic Electron Transport*, edited by Sohn, L. L., Kouwenhoven, L. P. & Schon, G., Series E: Applied Sciences (Kluwer Academic, Dordrecht), **345**, 105-214 (1997).
  - [4] Halperin, B. I. Quantized Hall conductance, current-carrying edge states and the existence of extended states in a two-dimensional disordered potential, *Phys. Rev. B* **25**, 2185-2190 (1982).
  - [5] Buttiker, M. Absence of backscattering in the Quantum Hall effect in multiprobe conductors, *Phys. Rev. B* **38**, 9375-9389 (1988).
  - [6] Chklovskii, D. B., Shklovskii, B. I. & Glazman, L. I. Electrostatics of edge channels, *Phys. Rev. B* **46**, 4026-4034 (1992).
  - [7] Tessmer, S. H., Glicofridis, P. I., Ashoori, R. C., Levitov, L. S. & Melloch, M. R. Subsurface charge accumulation imaging of a quantum Hall liquid, *Nature* **392**, 51-54 (1998).
  - [8] Yacoby, Y., Hess, H. F., Fulton, T. A., Pfeiffer, L. N. & West, K. W. Electrical imaging of the quantum Hall state, *Solid State Comm.* **111**, 1-13 (1999).
  - [9] Woodside, M. T., Vale, C., McEuen, P. L., Kadow, C., Maranowski, K. D. & Gossard, A. C. Imaging interedge-state scattering centers in the quantum Hall regime, *Phys. Rev. B* **64**, 041310(R) (2001).
  - [10] Hashimoto, K., Sohrmann, C., Wiebe, J., Inaoka, T., Meier, F., Hirayama, Y., Rømer, R. A., Wiesendanger, R. & Morgenstern, M. Quantum Hall Transition in Real Space: From Localized to Extended States, *Phys. Rev. Lett.* **101**, 256802 (2008).

- [11] Goldman, V. J. & Su, B. Resonant Tunneling in the quantum Hall regime : measurement of fractional charge, *Science* **267**, 1010-1012 (1995).
- [12] van Wees, B. J. *et al.* Observation of zero-dimensional states in a one-dimensional electron interferometer, *Phys. Rev. Lett.* **62**, 2523-2526 (1989).
- [13] Taylor, R. P., Sachrajda, A. S., Zawadzki, P., Coleridge, P. T. & Adams, J. A. Aharonov-Bohm oscillations in the Coulomb blockade regime, *Phys. Rev. Lett.* **69**, 1989-1992 (1992).
- [14] Kataoka, M. *et al.* Detection of Coulomb Charging around an Antidot in the Quantum Hall Regime, *Phys. Rev. Lett.* **83**, 160-163 (1999).
- [15] Camino, F. E., Zhou, W. & Goldman, V. J. Realization of a Laughlin quasiparticle interferometer: Observation of fractional statistics, *Phys. Rev. B* **72**, 075342 (2005).
- [16] Zhang, Y. *et al.* Distinct signatures for Coulomb blockade and Aharonov-Bohm interference in electronic Fabry-Perot interferometers, *Phys. Rev. B* **79**, 241304 (2009).
- [17] Giesbers, A. J. M. *et al.* Correlation-induced single-flux-quantum penetration in quantum rings, *Nature Phys.* **6**, 173-177 (2010).
- [18] Rosenow, B. & Halperin, B. I. Influence of Interactions on Flux and Back-Gate Period of Quantum Hall Interferometers, *Phys. Rev. Lett.* **98**, 106801 (2007).
- [19] Ihnatsenka, S. & Zozoulenko, I. V. Interacting electrons in the Aharonov-Bohm interferometer, *Phys. Rev. B* **77**, 235304 (2008).
- [20] Ihnatsenka, S., Zozoulenko, I. V. & Kirczenow, G. Electron-electron interactions in antidot-based Aharonov-Bohm interferometers, *Phys. Rev. B* **80**, 115303 (2009).
- [21] Hackens, B. *et al.* Dwell-Time-Limited Coherence in Open Quantum Dots, *Phys. Rev. Lett.* **94**, 146802 (2005).
- [22] Topinka, M. A. *et al.*, Imaging coherent electron flow from a quantum point contact, *Science* **289**, 232-2326 (2000).
- [23] Topinka, M. A. *et al.* Coherent branched flow in a two-dimensional electron gas, *Nature* **410**, 183-186 (2001).
- [24] Aoki, N., da Cunha, C. R., Akis, R., Ferry, D. K. & Ochiai, Y. Imaging of integer quantum Hall edge state in a quantum point contact via scanning gate microscopy, *Phys. Rev. B* **72**, 155327 (2005).
- [25] Crook, R. *et al.* Imaging Fractal Conductance Fluctuations and Scarred Wave Functions in a Quantum Billiard, *Phys. Rev. Lett.* **91**, 246803 (2003).

- [26] Woodside, M. T. & McEuen, P. L. Scanned probe imaging of single-electron charge states in nanotube quantum dots, *Science* **296**, 1098-1101 (2002).
- [27] Pioda, A. *et al.* Spatially Resolved Manipulation of Single Electrons in Quantum Dots Using a Scanned Probe, *Phys. Rev. Lett.* **93**, 216801 (2004).
- [28] Hackens, B. *et al.* Imaging and controlling electron transport inside a quantum ring, *Nature Phys.* **2**, 826-830 (2006).
- [29] Martins, F. *et al.* Imaging Electron Wave Functions Inside Open Quantum Rings, *Phys. Rev. Lett.* **99**, 136807 (2007).
- [30] Pala, M. G. *et al.* Local density of states in mesoscopic samples from scanning gate microscopy, *Phys. Rev. B* **77**, 125310 (2008).
- [31] Pala, M. G. *et al.* Scanning gate microscopy of quantum rings: effects of an external magnetic field and of charged defects, *Nanotechnology* **20**, 264021 (2009).
- [32] Folk, J. A. *et al.* Statistics and Parametric Correlations of Coulomb Blockade Peak Fluctuations in Quantum Dots, *Phys. Rev. Lett.* **76**, 1699-1702 (1996).
- [33] Baumgartner, A. *et al.* Quantum Hall effect transition in scanning gate experiments, *Phys. Rev. B* **76**, 085316 (2007).
- [34] Gildemeister, A. E. *et al.* Measurement of the tip-induced potential in scanning gate experiments, *Phys. Rev. B* **75**, 195338 (2007).
- [35] Das Sarma, S., Freedman, M. & Nayak, C. Topologically Protected Qubits from a Possible Non-Abelian Fractional Quantum Hall State, *Phys. Rev. Lett.* **94**, 166802 (2005).
- [36] Stern, A. & Halperin, B. I. Proposed Experiments to Probe the Non-Abelian  $\nu = 5/2$  Quantum Hall State, *Phys. Rev. Lett.* **96**, 016802 (2006).
- [37] Hackens, B. *et al.* Long dephasing time and high-temperature conductance fluctuations in an open InGaAs quantum dot, *Phys. Rev. B* **66**, 241305 (2002).
- [38] Gildemeister, A. E. *et al.* In situ treatment of a scanning gate microscopy tip, *Appl. Phys. Lett.* **90**, 213113 (2007).

## Acknowledgements

B. H. is postdoctoral researcher with the Belgian FRS-FNRS and F. M. is funded by FNRS and FCT (Portugal) postdoctoral grants. This work has been supported by FRFC

grant no. 2.4.546.08.F, and FNRS grant no 1.5.044.07.F, by the Belgian Science Policy (Interuniversity Attraction Pole Program IAP-6/42), This work has also been supported by the PNANO 2007 program of the Agence Nationale de la Recherche ('MICATEC' project). VB acknowledges the award of a 'Chaire d'excellence' by the Nanoscience Foundation in Grenoble.

### **Author contributions**

F. M. and B. H. performed the low-temperature SGM experiment; B. H., F. M. and V. B. analyzed the experimental data; L. D. and X. W. grew the InGaAs heterostructure; B. H. and C. A. D. processed the samples; B. H., S. F. and F. M. built the low temperature scanning gate microscope; B. H., F. M., S. F., H. S., S. H., M. P. and V. B. contributed to the conception of the experiment; B. H. and V. B. wrote the paper and B. H., F. M., H. S., S. H., M. P. and V. B. discussed the results and commented on the manuscript.

### **Competing financial interests**

The authors declare no competing financial interests.

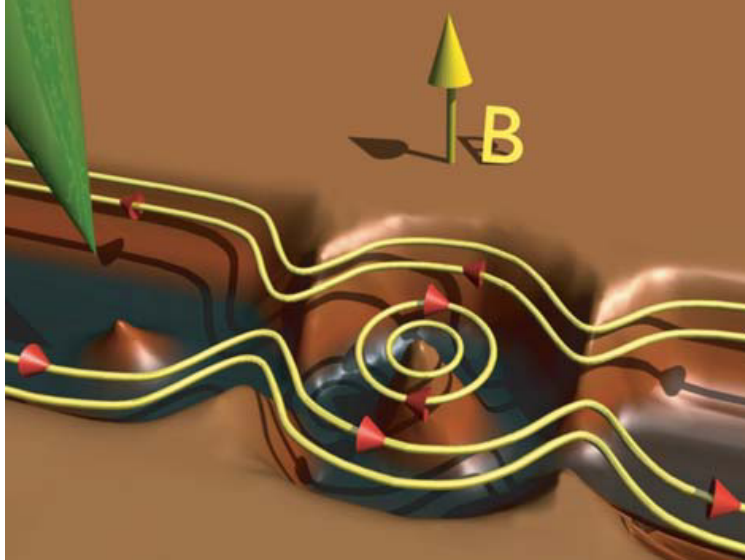


FIG. 1: **Artist view of edge states in the quantum ring confining potential.** To simplify, we have assumed that no edge state is reflected at the ring's openings, which may not be the case in the real quantum ring. The tip, in green, induces a local perturbation of the potential that can be scanned over the quantum Hall interferometer.

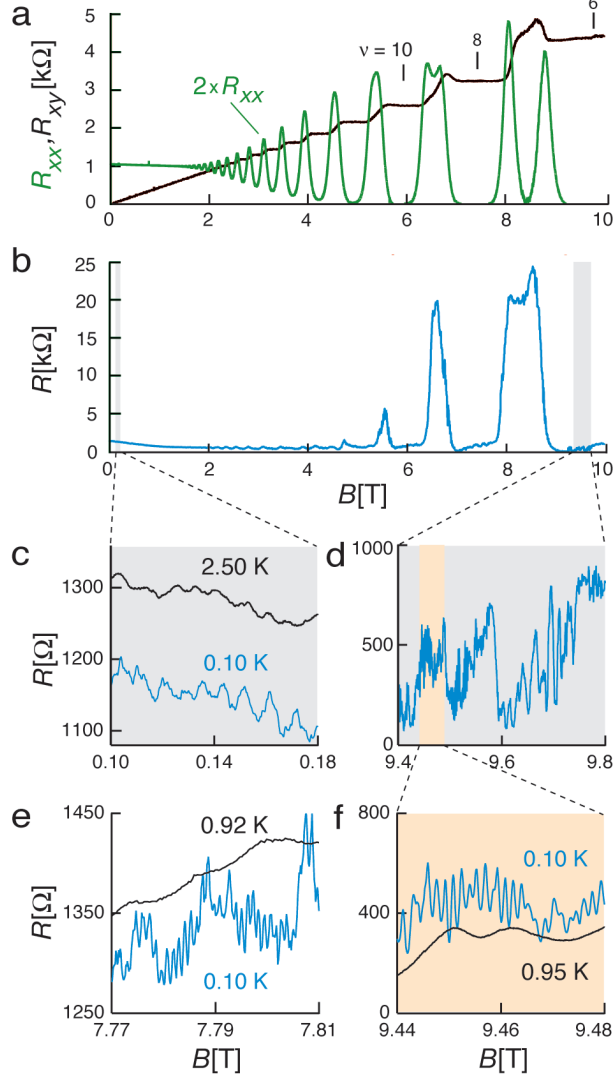


FIG. 2: **Magnetoconductance measurements on the Hall bar and on the quantum ring.**

(a) Longitudinal and transverse (Hall) resistances  $R_{xx}$  and  $R_{xy}$  vs  $B$ , measured in the Hall bar. Overshoots in  $R_{xy}$  originate from a mixing of the longitudinal and Hall resistances, due to a geometrical asymmetry of the Hall bar. (b) Magnetoconductance of the QR. (c) Low- $B$  magnetoconductance of the QR, measured at  $T = 0.1$  K and 2.5 K. The periodicity of the oscillations in  $R$  vs  $B$  is  $\Delta B = 9$  mT. (d) Magnetoconductance of the QR on the QH plateau around  $\nu = 6$ , at  $T = 0.1$  K. (e) Magnetoconductance of the QR on the QH plateau around  $\nu = 8$ ,  $T = 0.1$  K and 0.92 K. The periodicity of the oscillations in  $R$  vs  $B$  is  $\Delta B = 1.1$  mT. (f) Close-up view of Fig. 2d in the orange-shaded region, at  $T = 0.1$  K and 0.95 K. The periodicity of the oscillations in  $R$  vs  $B$  is  $\Delta B = 1.5$  mT.



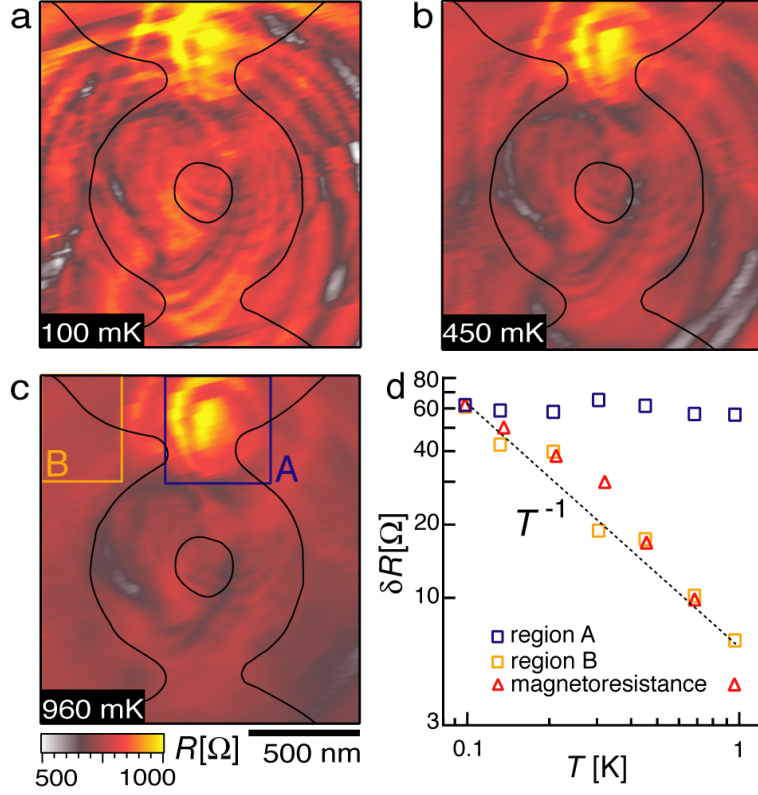


FIG. 3: **Scanning gate resistance maps of the quantum ring, showing Coulomb islands-related concentric rings.** (a-c)  $R(x, y)$  map obtained at  $B = 9.5$  T,  $V_{\text{tip}} = -1$  V and at  $T = 100$ , 450 and 960 mK, respectively. The black curves correspond to the position of the QR. (d)  $T$ -dependence of  $\delta R$ , calculated on raw  $R(x, y)$  maps in regions A and B defined on Fig. 3c (blue and orange squares, respectively) and on high-pass filtered  $R$  vs  $B$  traces (red triangles). The frequency of the high-pass filter on  $R$  vs  $B$  curves is  $60 \text{ T}^{-1}$ , and  $\delta R$  in this case is evaluated in the range 9.47 to 9.53 T.

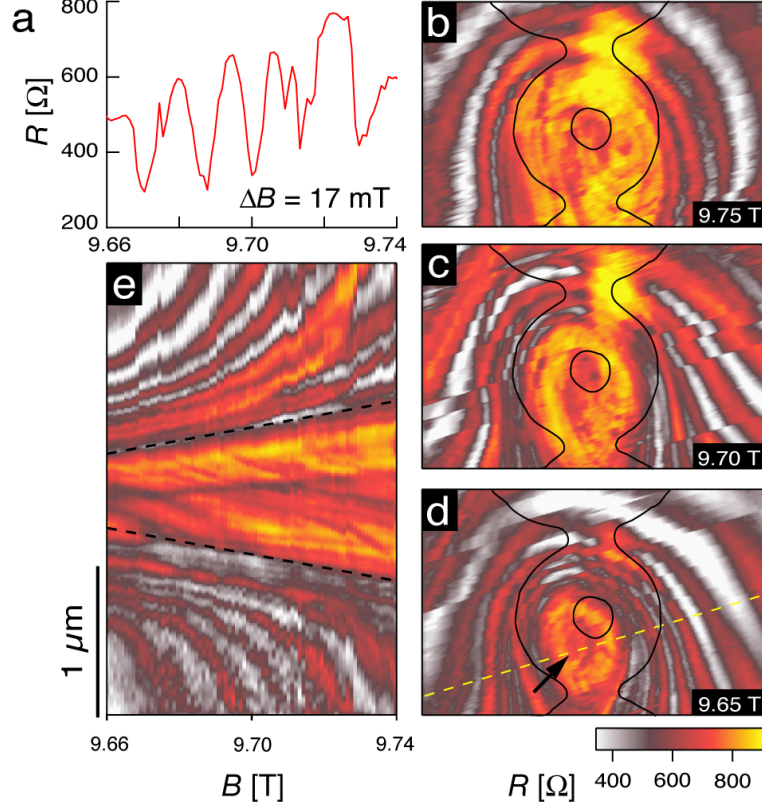


FIG. 4: Changing the magnetic fields reveals the position of a Coulomb island on scanning gate microscopy maps. (a)  $R$  vs  $B$  at  $T = 100$  mK. (b-d)  $R(x, y)$  maps obtained at  $B = 9.75, 9.70$  and  $9.65$  T, respectively, with  $T = 100$  mK and  $V_{\text{tip}} = -1$  V. (e)  $B$ -dependence of the  $R(x, y)$  profile measured along the dashed line in Fig. 4d.

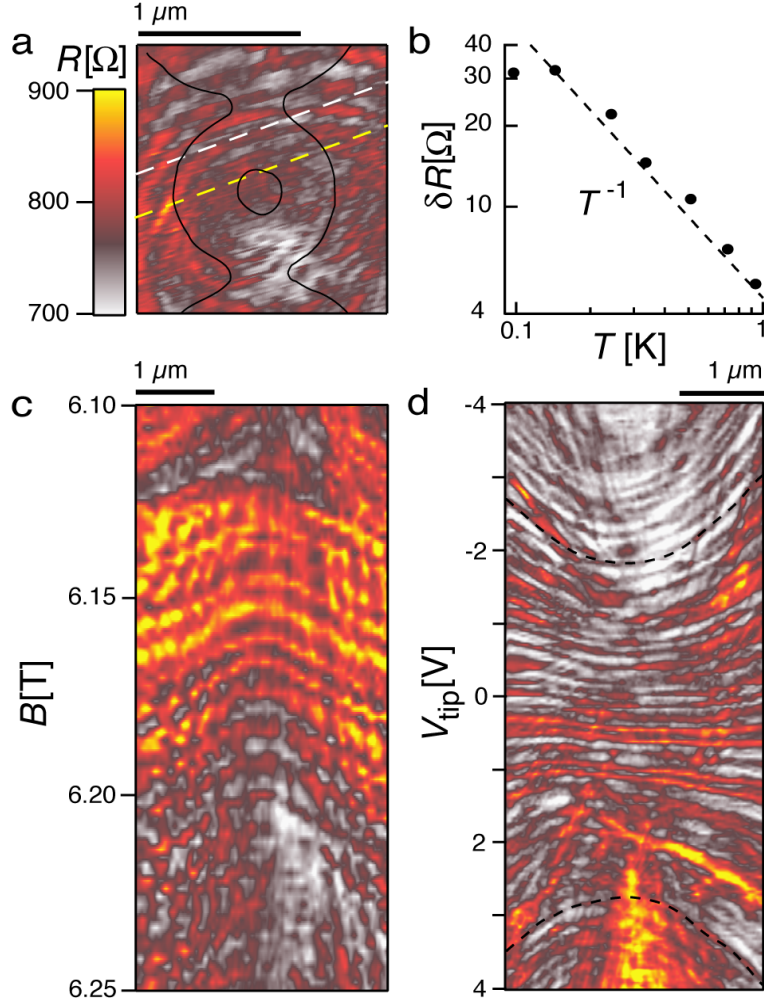


FIG. 5: **Shift of the Coulomb blockade resonances with the magnetic field and tip voltage.** (a)  $R(x, y)$  map measured at  $B = 6.25$  T and  $V_{\text{tip}} = -0.5$  V. (b)  $T$ -dependence of  $\delta R$  measured from a  $R(x, y)$  map at  $B = 6.25$  T. (c)  $B$ -dependence of the  $R(x, y)$  profile measured along the yellow dashed line in Fig. 5a. (d)  $V_{\text{tip}}$ -dependence of the  $R(x, y)$  profile measured along the white dashed line in Fig. 5a. The black line at the top of each graph represents  $1 \mu\text{m}$ .